

Original

Sassen, K.; Wang, L.; Starr, D.O.; Comstock, J.M.; Quante, M.:
**A Midlatitude Cirrus Cloud Climatology from the Facility
for Atmospheric Remote Sensing.**

Part V: Cloud Structural Properties

In: Journal of the Atmospheric Sciences (2007) AMS

DOI: 10.1175/JAS3949.1

A Midlatitude Cirrus Cloud Climatology from the Facility for Atmospheric Remote Sensing. Part V: Cloud Structural Properties

KENNETH SASSEN AND LIKUN WANG*

Geophysical Institute, University of Alaska Fairbanks, Fairbanks, Alaska

DAVID O'C. STARR

NASA Goddard Space Flight Center, Greenbelt, Maryland

JENNIFER M. COMSTOCK

Pacific Northwest National Laboratory, Richland, Washington

MARKUS QUANTE

GKSS Research Center, Geesthacht, Germany

(Manuscript received 19 August 2005, in final form 25 September 2006)

ABSTRACT

In this fifth of a series of papers describing the extended-time high cloud observation program from the University of Utah Facility for Atmospheric Remote Sensing, the structural properties of cirrus clouds over Salt Lake City, Utah, are examined. Wavelet analysis is applied to a 10-yr record of cirrus cloud ruby (0.694 μm) lidar backscatter data as a function of cloud height in order to study the presence of periodic cloud structures, such as the signatures of Kelvin–Helmholtz instabilities, cirrus mammata, and uncinus cells (all with length scales of $\sim 1\text{--}10$ km), as well as mesoscale cloud organizations generally believed to be induced by gravity waves. About 8.4% of the data display structures after passing a 95% confidence level test, but an 80% confidence level, which seems better able to resolve structures spread over long periods, yields 16.4%. The amount of identified cloud structures does not change significantly with length scale from 0.2 to 200 km, although the frequency of mesoscale cloud structures tends to increase as length scales increase. The middle-to-lower portion of cirrus clouds contains the most identified cloud structures, which seems related to the mesoscale organization of fall streaks from cloud-top-generating cells. The variability of cirrus cloud optical depth τ (defined by the standard deviation over mean τ) derived from a combined lidar and infrared radiometer (LIRAD) analysis is shown to be largely independent of τ . Because visual examination of the lidar displays also indicates that few cirrus layers can be considered horizontally homogeneous over our typical 3-h lidar data collection period, the authors conclude that the clouds in their sample are inherently inhomogeneous even though most cirrus structures are not revealed as periodic by wavelet analysis.

1. Introduction

Structure on many different scales is a fundamental attribute of all kinds of clouds. These cloud inhomogeneities have an impact on radiative transfer, and thus on

their role in climate. However, modeling weather and climate in general circulation models with current computer resources requires massive simplifications. Because of restrictions in model grid size and vertical atmospheric layer thickness, it is clear that many clouds in our atmosphere do not fit well into the modeler's grid cells. Clouds may not entirely fill the vertical layers or the horizontal boxes, and in any event are not likely to obey the plane-parallel horizontally homogeneous (PPH) assumption. Thus the effects of clouds must be treated implicitly using various subgrid-scale parameterizations. While this approach may be simple and

* Current affiliation: QSS Group, Lanham, Maryland.

Corresponding author address: Kenneth Sassen, Geophysical Institute, University of Alaska Fairbanks, 903 Koyukuk Drive, Fairbanks, AK 99775.
E-mail: ksassen@gi.alaska.edu

practical, it ignores the nonlinear relationship between cloud optical/microphysical properties and radiative quantities. Pioneering radiative model results (Harshvardhan and Randall 1985; Stephens 1985) pointed out that a significant bias can occur in radiative flux calculations without considering subgrid-scale cloud variability.

According to Várnai and Davies (1999), the radiative consequences of horizontal cloud inhomogeneity can be divided into two parts: the heterogeneity effect due to optical property variability, and the horizontal transport effect of photons that move between neighboring model columns. With regard to the first problem, Cahalan et al. (1994) proposed the independent pixel approximation (IPA) scheme, which divides the model grid box into independent pixels with separate optical/microphysical properties. Comparisons with Monte Carlo or other radiation transport simulations indicate that the IPA avoids many of the drawbacks of the PPH and is a good approximation in many cloud types, including cirrus (Liou and Rao 1996; Carlin et al. 2002). Nonetheless, only a three-dimensional radiation transfer scheme using a realistic cloud field can fully evaluate the IPA because of the side illumination due to slant photon paths and photon diffusion in the multiple scattering process. To help assess the various approaches, comprehensive measurements are needed to describe the typical structural variations in various types of atmospheric clouds.

Historically, research on the structure and formation mechanisms of cirrus clouds concentrated on the evident appearance of cirrus uncinus, which today are believed to be basic elements of more extended cloud fields (Sassen et al. 1989). Ludlam (1948, 1956) explained them based on ground observations as cell heads with a trailing hooklike structure resulting from wind shear effects. The size of the generation cells at top was estimated to be less than 1 km. Reuss (1967) and Yagi et al. (1968) based their research of uncinus structure on stereophotographic cloud cover methods and also emphasized the role of wind shear for cloud morphology. A twist of the uncinus tail with height was related to directional shear, as was earlier proposed by Oddie (1959). Observations by Yagi (1969) located the cirrus uncinus head in a turbulent layer with a dry adiabatic lapse rate, which allowed for its more convective appearance, while the fall streaks were situated in the stable layer below.

From more recent aircraft, lidar, and radar studies, we know that a variety of structures (i.e., cloud microphysical inhomogeneities) occur in cirrus clouds on both the cloud scale (generally <10 km) and the generally larger mesoscale. These structures reflect the on-

going or frozen effects of dynamical processes involved in cloud formation, maintenance, and dissipation; that is, of vertical air motions and their organizations, and the vertical shear of the horizontal wind velocity. Cirrus clouds are regarded as a highly coupled microphysical–radiative–dynamical system (Quante and Starr 2002), where many nonlinear interactions can occur. Cloud structures linked to various scales of vertical motions include cloud-top uncinus generating cells (Heymsfield 1975) and their organization into mesoscale uncinus complexes (Sassen et al. 1989), gravity waves (Starr et al. 1992; Gultepe and Starr 1995; Sassen 2002), Kelvin–Helmholtz (KH) instabilities (Sassen 1995; Sassen et al. 2003a), and cirrus mammata (Wang and Sassen 2006). Such structures visible in lidar displays will be illustrated and discussed in the following section. Turbulence is another cause of inhomogeneities in cirrus that has been studied with aircraft probes (e.g., Gultepe and Starr 1995; Gultepe et al. 1995; Smith and Jonas 1997; Quante and Starr 2002), but turbulence typically exists at scales too small to be effectively probed in cirrus by lidar or radar.

In this study, we apply statistical analysis to height versus time records of range-corrected, attenuated lidar backscattering from numerous single-layer cirrus clouds to study the cloud inhomogeneities that modulate radiation transfer through clouds. (Cloud field inhomogeneity with respect to the vertical overlap of broken layers is not addressed here.) The data were collected from the University of Utah Facility for Atmospheric Remote Sensing (FARS). The time and height variations in laser backscatter are due to changes in cloud microphysical content, and are related to optical properties such as the attenuation coefficient by a constant that depends essentially on particle shape. For the lidar used predominantly here, the backscattered power corresponds to a relatively small volume of cloud (e.g., a column ~2 m in diameter and 3.75 m in length at 10-km altitude). Such samples are repeated every 10 s (or 12 s) to form a time series of vertical signal profiles. Because the lidar cloud backscatter is predominantly in the geometrical optics domain, it is proportional to the total cross-sectional areas of the ice crystals in the instantaneous scattering volume. In other words, we assume that variations in the lidar signal with time and height are a proxy of the variations in solar scattering that would be experienced in inhomogeneous ice clouds. The structures detected here reflect the formation processes in cirrus, and preserve the effects of recent wave motions.

The laser backscattering fields are processed by wavelet analysis at height-resolved intervals to determine the presence of cloud structures over the range of

permissible periods (converted to scale lengths using interpolated radiosonde wind speed data at each height). Wavelet analysis has the advantage over Fourier methods in that temporally restricted, periodic wave packets yield strong spectral signatures over the times that they occur (i.e., they are locally periodic) regardless of their permanency in the cloud field. This method individually resolves coexisting periodic signal variations on multiple scales (Torrence and Compo 1998), as we will illustrate. We also use the time variations in visible cloud optical depth τ obtained from a previous LIRAD analysis (Sassen and Comstock 2001) to directly determine the optical variability in cirrus. This analysis is applied to a large portion of the FARS high cloud dataset to obtain statistical properties on all types of cirrus structures, whereas more detailed findings from various structures will be reported elsewhere.

2. Cirrus cloud structures: An overview

Waves are a common feature in the atmosphere, and occur over a large range of wavelengths, or scale lengths, stretching from the planetary scale down to hundreds of meters. The waves that influence cirrus clouds on the mesoscale are internal gravity waves (or inertia gravity waves if Coriolis forces play an important role). Waves may be involved in the cirrus formation process, and can influence the appearance of cirrus cloud fields and the internal microphysical structure. Under certain conditions internal gravity waves can become convectively unstable and break up, which generates turbulence that acts as a mixing agent to smaller scales. This often happens when inertia gravity waves interact with shear layers (Uccellini and Koch 1987; Dunkerton 1997; Lane et al. 2004), which at midlatitudes frequently appear in conjunction with jet streams. The most obvious sources for gravity waves are topography, convection, and wind shear (Nastrom and Fritts 1992; Fritts and Alexander 2003). The signature of gravity wave effects on or within clouds can survive long after they originally form. Observational studies of mesoscale structures in cirrus (see Table 1) reveal the action of gravity waves (Starr et al. 1992; Gultepe and Starr 1995), orographically induced waves (Sassen 2002), and the organization of cirrus uncinus cells into mesoscale uncinus complexes (MUC; Sassen et al. 1989).

In addition to cirrus cloud structures organized on the mesoscale, we illustrate in Fig. 1 the presence of cirrus uncinus, KH waves, and cirrus mammata that are often present in lidar height versus time backscatter

displays. We refer to these as cirrus cloud-scale structures, generally with length scales of <10 km. Shown from top to bottom are displays of cloud-top cirrus uncinus cell heads with long, delicate, sheared crystal tails, KH waves embedded at several levels, and pronounced cirrus mammata protruding below the cloud base. Table 1 summarizes our knowledge of the length scales associated with these cloud-scale and mesoscale structures from a number of previous cirrus cloud observational studies.

Cirrus uncinus generating cells generally occur at the cirrus cloud top (or other unstable layer) where convective instabilities may be present (Heymsfield 1975; Auria and Campistron 1987). The fallstreaks they generate can often descend many kilometers in the vertical. The cell heads are typically separated in space by a few kilometers, but high-resolution lidar observations indicate that the cell heads themselves may be composed of a series of much smaller structures (Sassen 2002). Kelvin–Helmholtz instabilities (i.e., a shear instability) are a type of mechanically generated wave that occurs in cirrus regions with strong wind shear (Sassen et al. 2003a). These typically have wavelengths on the order of a few to several kilometers and may grow and break up quickly, leaving patches of turbulence behind. Finally, like thunderstorm mammata, their cirrus counterparts are found where the cirrus cloud base descends into dry subcloud air (Sassen et al. 2001; Wang and Sassen 2006). Density currents associated with ice particle evaporation appear to set up the undulations in the cloud-base region.

3. FARS dataset and signal processing

The extended FARS high cloud dataset, which supported the First International Satellite Cloud Climatology Project (ISCCP) Regional Experiment (FIRE), has been described in the previous four parts of this series of papers. In this study we rely on findings derived from statistical analyses of data obtained by the turnkey cloud polarization lidar (CPL), based on a high-power (1.5 J), 0.1-Hz, ruby (0.694 μm) laser transmitter and dual backscatter detector channels with 7.5-m range resolution (Sassen et al. 2001). Although ruby lidar data collection at FARS (40°49'00"N, 111°49'38"W) commenced in 1987 and ended in early 2002, various subsets of the data have been used according to the lidar data characteristics and the availability of complementary data. In the other parts of this series of papers, we have examined the macrophysical/synoptic (Sassen and Campbell 2001), cloud microphysical (Sassen and Ben-

TABLE 1. Cirrus cloud structures observed in previous field studies.

Author	Inhomogeneous structure	Length scale (km)	Instruments	Comments
Heymsfield (1975)	Uncinus generating cell	1–2	Radar and aircraft	Minnesota, Illinois, Colorado, Wyoming
Auria and Campistron (1987)	Cirrus generating cell	1.3 and 0.7	Radar	Spain, 1987
Sassen et al. (1989)	MUC	~15–~100	Lidar, radar, and aircraft	Utah, Colorado, Wisconsin, 1983–86
Starr and Wylie (1990)	Cirrus uncinus cell	~1	Radiosonde and satellites	Wisconsin, 1986
	MUC	20–500		
Sassen et al. (1990)	Cellular structure	~120	Lidar and aircraft	Wisconsin, 1986
	MUC			
Grund and Eloranta (1990)	Cirrus uncinus cell	~1	Lidar	Wisconsin, 1986
	MUC	4–12		
Smith et al. (1990)	Two-dimensional eddies		Aircraft	Wisconsin, 1986
Starr et al. (1992)	Gravity wave	40	Airborne lidar	New Jersey, 1985
Gultepe and Starr (1995)	Small-scale convective cells	2–9	Aircraft	Wisconsin, 1986
	Gravity waves	10–20		
	Quasi-two-dimensional waves	100		
Gultepe et al. (1995)	Coherent structure	0.2–10	Radar and aircraft	Kansas, 1991
Sassen (1995)	Kelvin–Helmholtz wave	3.1	Airborne lidar	Coral Sea, 1993
Demoz et al. (1998)	Convective cell	1.2	Aircraft	Oklahoma, 1996
	Gravity waves	2–40		
Sassen et al. (2001)	Mammata		Lidar	Utah
Quante et al. (2002)	Fall streaks		Lidar and radar	Germany, 1997 Oklahoma, 1996
	Generating cell			
Sassen (2002)	Mammata		Lidar	Oklahoma, Utah, 1992–1999
	MUC			
Sassen et al. (2003a)	Orographic waves			
Wang and Sassen (2006)	Kelvin–Helmholtz wave	2.45	Lidar	Oklahoma, 1997
	Cirrus mammata	2.9	Lidar	Utah, 1992–2002

son 2001), radiative (Sassen and Comstock 2001), and halo-producing (Sassen et al. 2003b) properties of these midlatitude cirrus clouds. Note that the types of clouds probed by FARS instruments were visually identified and recorded in field notes, and regularly characterized with fisheye photographs within the context of a typical 3-h observation period.

Here we use a subset of 2208 h of CPL data collected from 1992 to 2002. Over this period, laser shots were typically digitized once every 10 s, or every 12 s in the case of the highest cirrus clouds that required longer processing times. Thus, with regard to the average cirrus-level wind velocity of $\sim 20 \text{ m s}^{-1}$ (Sassen and Campbell 2001), the typical minimum and maximum resolvable advected cloud distances are about 0.2 and 200 km, respectively. Although cloud variations related to turbulence at shorter scales and synoptic activity at longer scales are not represented in this dataset, much of the

domain of cirrus cloud-scale and mesoscale waves is captured. Figure 2 provides the yearly, monthly, and hourly distributions of this dataset in order to explore potential data collection biases. Note that the data collection schedule favored local afternoon/evening orbiting satellite overpasses when cirrus clouds were present. However, to facilitate the statistical analyses of the data in the current application, both visual screening and special data processing schemes were used.

The visual screening attempted to remove unsuitable data from the routine wavelet analysis. To trustfully identify the structural properties of cirrus clouds using the range-normalized attenuated backscatter (hereafter, lidar backscatter), lidar records were rejected if the cirrus layer was influenced by strong attenuation (shadowing) from denser elements within the cirrus or by variable lower clouds, or if insufficient cirrus data were recorded. The remaining dataset contained 1382 h of

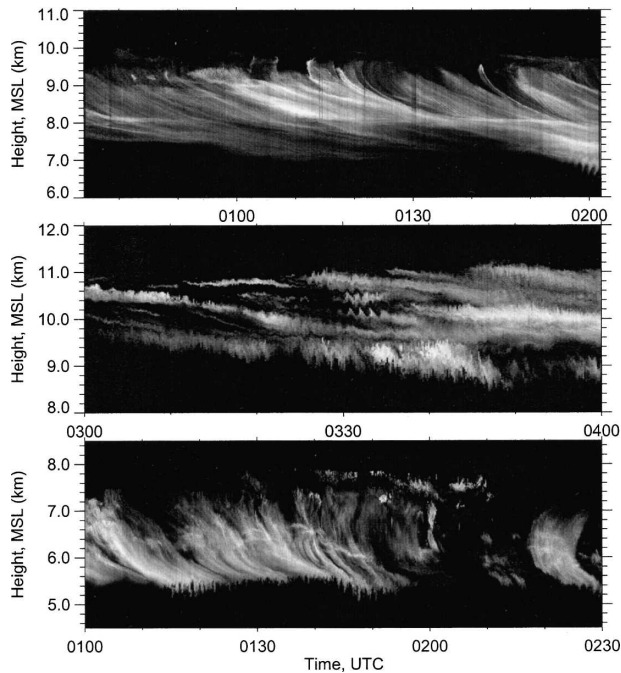


FIG. 1. Representative CPL height vs time displays of lidar backscatter from (top to bottom) cirrus uncinus cells, Kelvin-Helmholtz waves, and cirrus mammata, collected at FARS at the indicated times on 15 Apr 1995, 4 Apr 1993, and 7 Dec 1992, respectively.

cirrus observations derived from 533 independent cirrus cloud fields, or 62.6% of the total data recorded over the 10-yr period.

Before analysis the data were processed to improve data quality. First, any short gaps (up to four missing shots) in the lidar data record were filled in by interpolation using the neighboring vertical signal profiles. To limit the effects of random signal noise on the analysis and at the same time reduce the computational burden, five lidar shot data points were averaged to yield 37.5-m vertical resolution between cirrus cloud base and top heights. (No temporal averaging was done in order to maintain the maximum possible time resolution and identify the shortest possible length scales.) Sensitivity tests showed that this amount of averaging effectively reduced the effects of signal noise, but did not overaverage and destroy the smallest-scale structures that could be visually identified in the lidar height-time displays at the given measurement resolutions (Wang 2004).

4. Statistical methodologies

The procedure to characterize cirrus cloud inhomogeneities from time and height variations in lidar back-

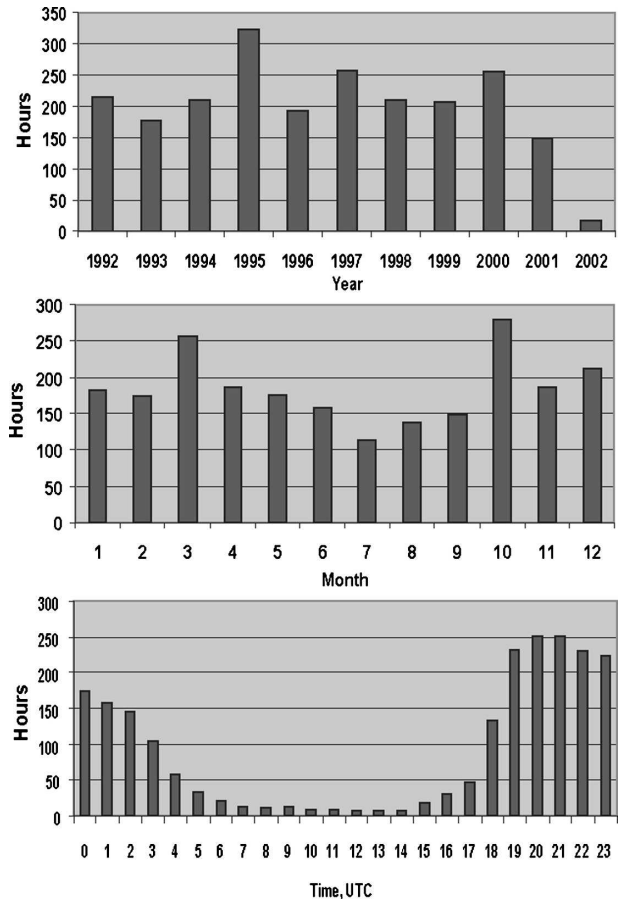


FIG. 2. Temporal breakdown of the accumulation of FARS CPL observations from 1992 to 2002 in terms of (a) year, (b) month, and (c) hour UTC.

scatter is shown in the flowchart of Fig. 3 [see Wang (2004) and Wang and Sassen (2006) for further details]. It begins with the horizontal returned power slice at the lowest cloud-base altitude and ascends to the cloud top at 37.5-m height intervals while performing the wavelet analysis described below. Five main steps are involved in the algorithm including: 1) preliminary data processing, 2) cloud boundary detection, 3) wavelet analysis, 4) confidence testing, and 5) combining the data into a two-dimensional (2D) cloud data product for further study. Although in the cloud height-dependent wavelet analysis the interpolated sounding wind speed is used, for the 2D cloud data product the mean horizontal wind velocity from cloud base to cloud top is used to transform the time period into an average length scale. The cloud boundary values are acquired using the lidar signal algorithm developed by Wang and Sassen (2001).

Below we focus on the last three steps of the analysis program. A cirrus cloud case study observed by the CPL at FARS on 17 October 1992 shown in Fig. 4

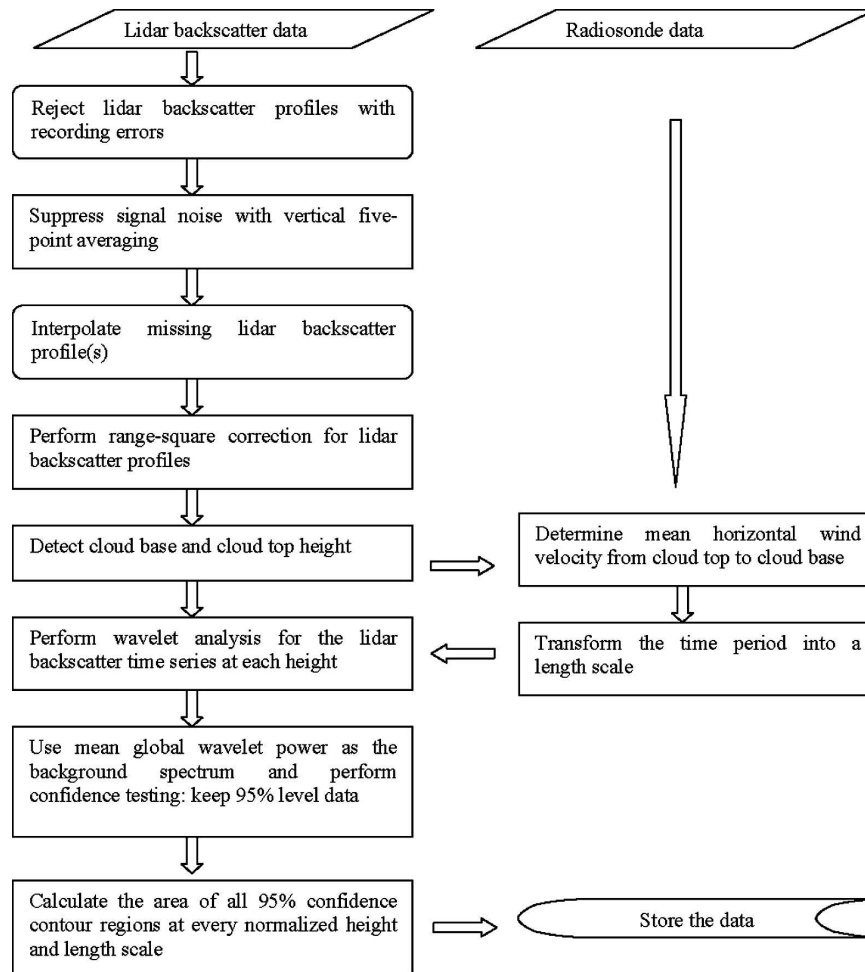


FIG. 3. Flowchart illustrating how the lidar backscatter is processed to derive the inhomogeneities in the structure of cirrus clouds.

illustrates the data analysis methods. The height versus time display of laser backscatter at top shows obvious structures organized from the mesoscale (i.e., the several serrated structures), to the uncinus cells and mammata cloud-scale features. Note that to the right of the lidar display are given the temperature and wind profiles derived from the closest Salt Lake City radiosonde. Descriptions of the testing and choice of statistical confidence levels are presented in the appendix.

a. Wavelet transform

The time series of lidar backscatter in each consecutive height interval are input into the continuous wavelet transform (CWT) algorithm to calculate the wavelet spectrum representative of a horizontal cloud slice. The wavelet transform (WT) method is a popular technique within the meteorological community for data analysis, including atmospheric turbulence, climate time series,

convective organizations, and inhomogeneous cloud structures (e.g., Farge 1992; Torrence and Compo 1998; Demoz et al. 1998; Quante et al. 2002). Specifically, if the signal $X(t)$ belongs to a square-integrable function, the CWT is defined as

$$\widehat{W}(\tau, s) = \frac{1}{(s)^{1/2}} \int_{-\infty}^{+\infty} X(t) \psi^* \left(\frac{t - \tau}{s} \right) dt, \quad (1)$$

where $\psi(t)$ is the element transform wavelet function referred to as the mother wavelet defined by the translation and scale parameters, τ and s , respectively:

$$\psi_{\tau,s}(t) = \frac{1}{(s)^{1/2}} \psi \left(\frac{t - \tau}{s} \right). \quad (2)$$

For our application, a Morlet wavelet function with a wavenumber $w_0 = 6$ is chosen as the mother wavelet

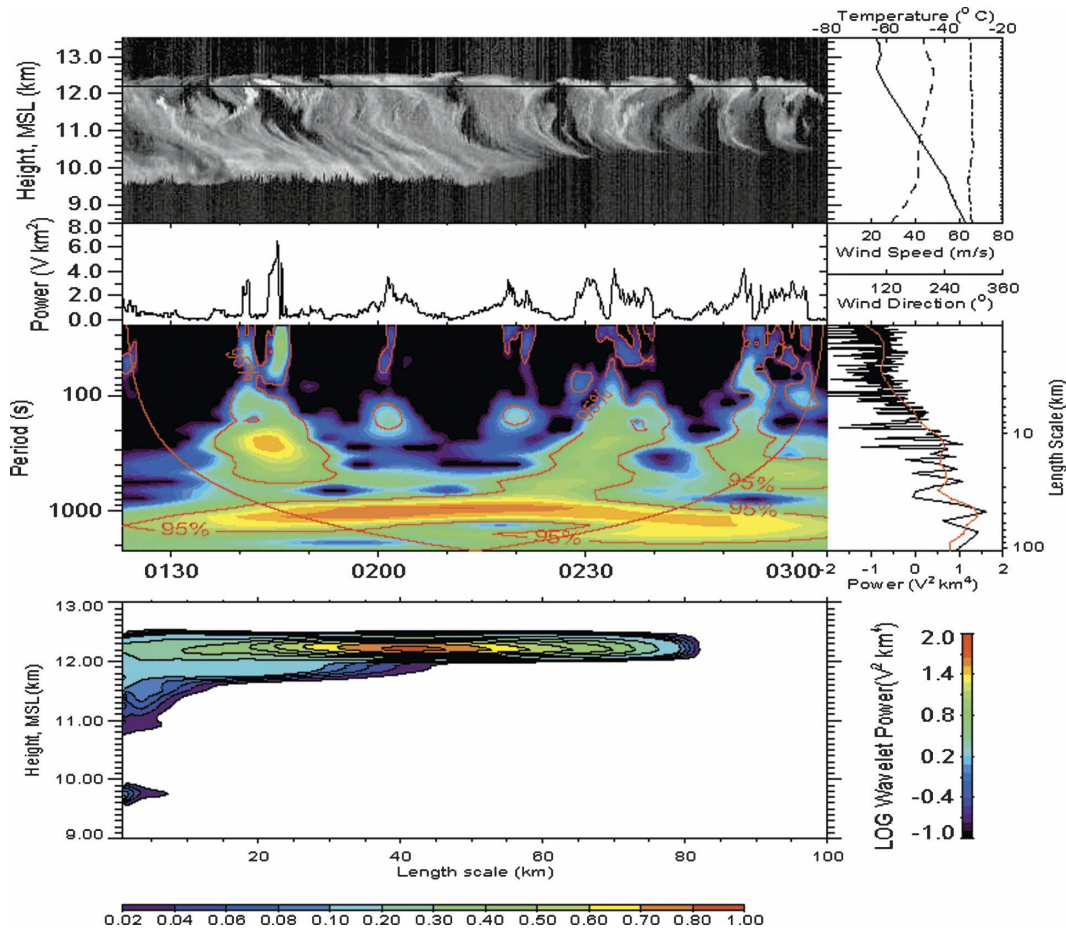


FIG. 4. FARS cirrus case observed by the CPL on 17 Oct 1992 to illustrate the wavelet analysis method: (a) lidar height-time backscatter image displayed using a logarithmic grayscale, with local radiosonde temperature (solid), wind speed (dashed), and direction (dot-dashed) profiles; (b) the horizontal lidar backscatter variations at 12.19-km height; (c) the corresponding wavelet spectra with contours showing the 95% confidence level finding, with Fourier (black line) and global wavelet (red line) analyses at right; and (d) the percentage of the 95% confidence level area relative to the total cloud area given as a function of length scale (derived from the mean cloud-level wind speed) and cloud height.

function. The Morlet wavelet is a sine and cosine function modulated by a Gaussian function and defined as

$$\psi_0(\eta) = \pi^{-1/4} e^{i\omega_0\eta} e^{-\eta^2/2}, \quad (3)$$

where ψ_0 is the wavelet value at nondimensional time η . Compared with other wavelet functions that favor individual event localization (e.g., Mexican Hat), the Morlet wavelet is a locally periodic wave train that is appropriate for spectral accuracy. This mother wavelet is well suited to detect wave packets with only a few undulations, which has proved to be useful for the situation in cirrus clouds. A complete description and detailed information on the codes is given in Torrence and Compo (1998).

By decomposing the lidar backscatter through wave-

let transform, we construct a combined image of the energy as a function of time, wavelet scale (or frequency), and corresponding height. The next step is to identify the more significant wavelet energy peaks that correspond to obvious (i.e., visually identified) cirrus cloud structures (see appendix). To determine significant levels for either Fourier or wavelet spectra, an appropriate background spectrum must first be chosen. By assuming that different realizations of geophysical processes will be randomly distributed above this background, one can then compare the actual spectrum against that of a fully random distribution (Chatfield 1996). The null hypothesis is defined for the confidence testing of the wavelet power as follows. If the time series have a mean background power spectrum, a peak in the wavelet power spectrum significantly above this

background spectrum can be assumed to represent a true feature with a certain confidence level. Further assuming that the wavelet coefficients are normally distributed above the background spectrum (Torrence and Compo 1998), the wavelet spectrum will be chi square distributed with two degrees of freedom (Wilks 1995).

In choosing the appropriate background spectrum for significance testing, it is known that the spectra for many geophysical time series have features of red noise, which has increasing power with decreasing frequency resulting in a negative slope of the power spectrum (Gilman et al. 1963). Percival (1995) showed that the global wavelet spectrum provides an unbiased and consistent estimation of the true power spectrum of a time series. Thus, the global wavelet spectra provide a useful measure of the background spectrum, against which peaks in the local wavelet spectra can be tested (Torrence and Compo 1998). In addition, the time-averaged global wavelet spectrum also has the characteristics of red noise and thus can be treated as an appropriate background noise spectrum. In the method applied here, all the global wavelet spectra of cloud lidar backscatter are averaged as the background noise spectrum.

Figure 4c provides an example of confidence testing results of the local wavelet power for the horizontal lidar backscatter slice centered at 12.19 km. (Note the horizontal line in the lidar display at top and the corresponding signal plot below.) To the right of the wavelet analysis are given for comparison the power spectra from the standard Fourier (black line) and global (i.e., average power) wavelet approaches. The color scale for the log of wavelet power is shown to the right of the bottom panel. The mean horizontal wind velocity of 43.8 m s^{-1} at this height was used to transfer the time period into a length scale (both scales are given in the color wavelet analysis panel). The 95% confidence level contours shown in this case identify mesoscale uncinus complexes with ~ 50 -km horizontal scale, while those at 5–10 km another mesoscale organization. The uncinus cells near cloud top are revealed by the 95% contours with 1–3-km length scale. These scale lengths also show up in the global wavelet (red line) and Fourier power spectra analyses. Thus, the wavelet transform with appropriate confidence testing can successfully and efficiently characterize the periodicity of cloud structural variations through the analysis of lidar backscatter. Figure 4d is discussed below.

b. Combined 2D cloud data product

The wavelet spectra within the 95% confidence level contours, for example, are obviously a function of time, period or length scale, and height. To simplify the

wavelet transform results for each cloud field, the percentage of how many data points (relative to the total cloud sample) at every length scale that fall into a confidence level can be calculated. However, those data points outside the cone of influence (the curved red line in Fig. 4c), which are affected by the finite end points of the time series, are not counted because they may not reflect valid structures, even if they are above the selected confidence level compared with the background spectrum. In other words, only the samples that fall within the 95% confidence level contours and in the region above the cone of influence curve are surveyed in this case.

With reference to the color scale bar at bottom, the percentage distribution of the 95% confidence level area as a function of cloud height and length scale is given in Fig. 4d for the entire cloud. The mesoscale structures with a length scale of 30–50 km, making up 70%–100% of the valid samples, are dominant near cloud top. At the cloud base, the existence of the local maximum area with length scales of smaller than 5.0 km indicates the cirrus mammatus structures visible in Fig. 4a from 0140–0200 UTC. The upper cloud region has relatively stronger structural characteristics than the cloud-base region in this case.

c. Direct cirrus cloud optical depth analysis

As described above, the horizontal variations in lidar signals (affected by attenuation) caused by cloud microphysical variations are used here as a proxy of the structures occurring in cirrus. However, this analysis cannot yield quantitative information on the strengths of cloud inhomogeneities with regard to photon transport in the vertical or horizontal directions. To address this, we need to know the variability in τ , which is used as a basic parameterization in radiation transfer calculations in large-scale models (Barker 1996). Thus, we have reanalyzed the cirrus cloud τ dataset calculated using the LIRAD method based on an overlapping FARS cirrus cloud dataset (Comstock and Sassen 2001), which has a maximum uncertainty in τ of about 30%. (The presence of zero τ in cloud gaps is included in the analysis, and, as above, the dataset was screened to remove those cases that had gaps in temporal coverage due to the effects of lower, blocking clouds.) We compute the mean τ for each cirrus case and then determine its standard deviation σ , where the cirrus optical variability is expressed by σ/τ (Smith and DelGenio 2001). Although this is a direct indicator of cirrus cloud τ variability in the zenith direction, the lidar profiles were averaged over 2-min intervals to reduce signal noise effects, and so are coarser than the 10- or 12-s intervals used in the wavelet study.

d. Uncertainties

Sources of uncertainties in this study include those related to lidar signal characteristics, and determining a wavelet transform approach and confidence level (see appendix) that can satisfactorily identify valid cirrus cloud structures. Generally, however, lidar signal-to-noise issues are unimportant because of the much larger dynamic range of signals associated with structurally related cloud backscattering variations compared to signal noise (Qiu and Er 1995), as well as the signal preprocessing methods employed. Problems affecting the integrity of the wavelet analysis reflect the fact that cirrus clouds are not generally static with time. The wave motions responsible for cirrus cloud inhomogeneities leave behind structures that will decay with time according to various processes such as turbulence, wind shear, and to evolving microphysical changes from associated radiative or other feedbacks.

Thus, a fundamental problem is related to our dependence on satisfying the Taylor hypothesis, which is valid only when the mean cloud advection speed is greater than the local cloud development time scale. If this condition is violated, ambiguous results can occur particularly under conditions involving long lidar data records with low and variable wind speeds within the cirrus. Because local cirrus-level wind data are only available from the National Weather Service at 12-h intervals, it can be assumed that errors in the conversion from period to length scale are generally present to some degree. Such factors indicate that it is the short-term periodic cloud structures that are detected at the highest confidence levels, while the identification of larger wavelength mesoscale patterns, which require longer period data records, will be less certain. As discussed in the appendix, for some purposes we use both 95% and 80% confidence levels.

5. Case studies

In this section are displayed wavelet analyses of three common types of visually identified cirrus cloud structures. As in Figs. 4 and A1, Figs. 5–7 illustrate how wavelet analysis can detect both cloud-scale features and their organization into, or coexistence with, mesoscale elements. In each case the same format as in Fig. 4 is used, which provides comparisons of the 95% confidence level findings with Fourier and global wavelet analyses.

The upper part of Fig. 5 depicts the analysis of a horizontal cirrus cloud slice through KH wave instabilities, visible particularly at right. These waves occur in a region of strong horizontal wind shear. The wavelet and other statistical findings show significant cloud organi-

zations on the order of a few kilometers due to uncinus fallstreaks, the KH wave packets at ~ 10 km, and the mesoscale organizations at ~ 100 km. The bottom panel shows that the mesoscale structures are particularly prevalent (i.e., they are present 60%–70% of the time near cloud base), in comparison to the amounts of uncinus cells and KH waves that are more temporally confined.

The classic example of cirrus mammata given in Fig. 6 finds that these structures are periodic on a ~ 1 -km scale length. Within the entire cirrus cloud (bottom panel), there is evidence for mesoscale organizations on the order of ~ 30 and 80 km. Note that the analysis in this case is complicated by the apparent signal loss above ~ 8.5 -km height due to laser pulse attenuation in the particularly dense cirrus from 2200 to 2300 UTC.

The final example in Fig. 7 is derived from 10-Hz pulse repetition frequency polarization diversity lidar (PDL; Sassen et al. 2001) measurements of a 3.0-km-deep cirrus layer containing a variety of cloud structures. These include at midcloud level cirrus uncinus cells and their complexes, and what appear to be cirrocumulus cells near cloud top. The vertically resolved analysis in the bottom panel identifies the cloud top and cloud base combined cloud-scale and mesoscale structures, as well as the cloud-scale cirrus uncinus cells at ~ 12 -km height.

6. Mean properties of cirrus cloud-scale structures

Table 2 provides pertinent data on the mean properties and the range of length scales deduced from the FARS dataset. Note that the mammata and KH wave statistics are based on analyses of 30 and 27 CPL cirrus cases, respectively. Although mammata occur commonly when the cirrus cloud base descends into dry air layers (Wang and Sassen 2006), KH waves are much less frequently seen in the lidar displays. Only 19 KH case studies, involving 27 wave packets, were identified in the 10-yr dataset, but this may reflect the relative lack of permanency of these features. For the commonly observed uncinus cells, we rely on the single case study shown in Fig. 7 probed by the higher resolution PDL, because the CPL measurements may fail to fully resolve these relatively small cloud features under low wind speed conditions.

The mean height and temperature values in Table 2 support the notion that uncinus cells, KH waves, and mammata are generally found at cloud top, embedded in cloud, and at cloud base, respectively. Although mammatus complexes typically extend over long distances, KH waves tend to occur in relatively small groups. In the single uncinus case studied by the PDL,

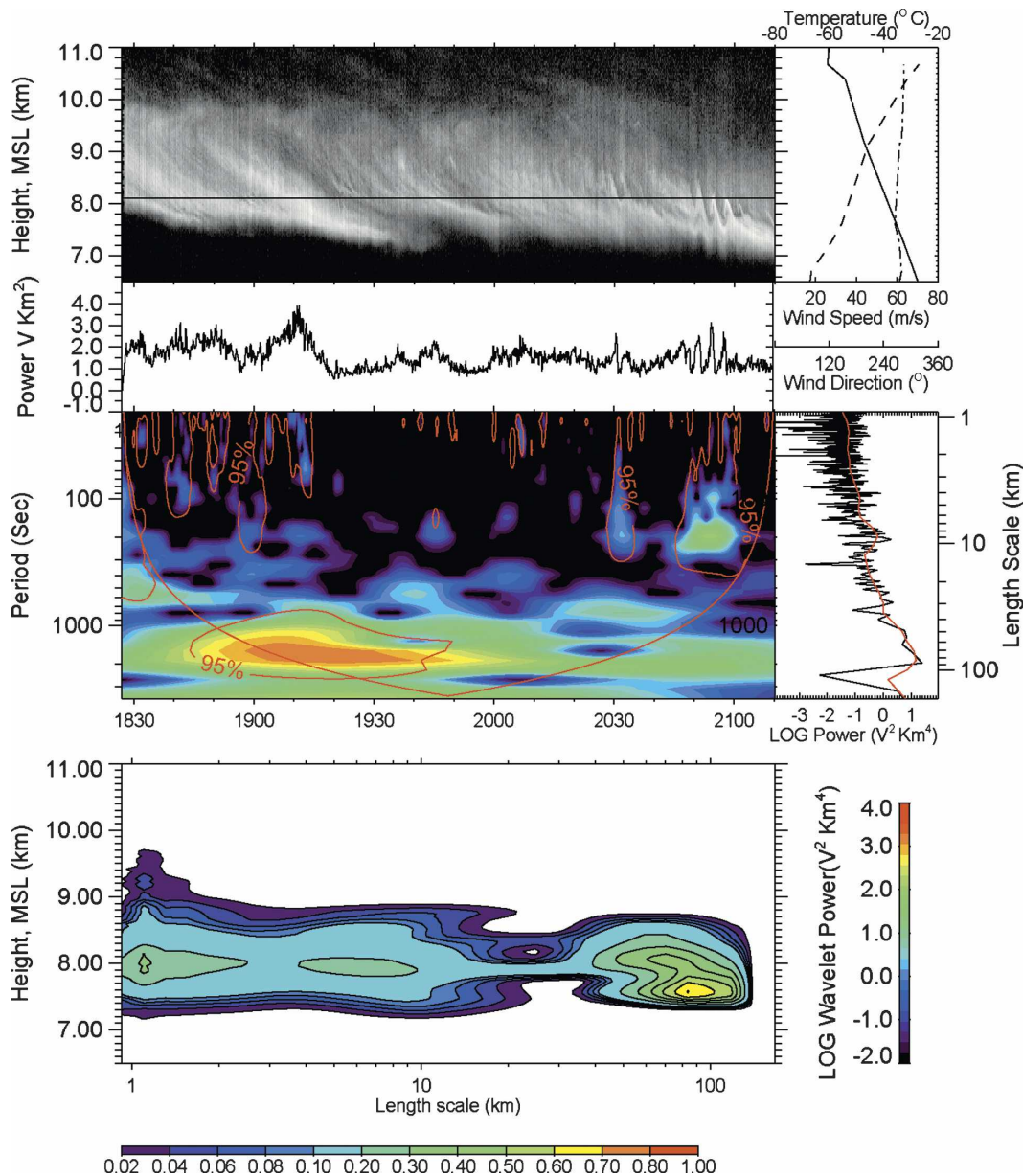


FIG. 5. As in Fig. 4, except that the height of the wavelet analysis is chosen to sample the KH waves in the lidar backscatter display at right, collected on 23 Jan 2000.

30–40-km mesoscale uncinus complexes were found. The maximum depths of both mammata and KH waves are similar, while uncinus cell heads are difficult to separate from their precipitation tails, which can extend for many kilometers below the cells and so are not reported in Table 2. In terms of their length scales, all three structures have mean and maximum values of 2.0–4.5 km and $< \sim 10$ km, respectively. These cirrus cloud scales are smaller than the typical mesoscale cloud organizations often apparent in the lidar displays, as has been illustrated in our cirrus case studies.

7. Climatological cirrus structural analyses

a. Total cirrus sample

Our approach is based on the three analysis steps (preliminary data processing, application of wavelet transform throughout the cloud, and confidence testing), followed by combining the results into a single 2D display representative of each cirrus cloud case study. Although Figs. 4–7 present examples of this analysis applied to selected case studies, the total cirrus cloud sample is comprised of 533 independent cases. Figure 8

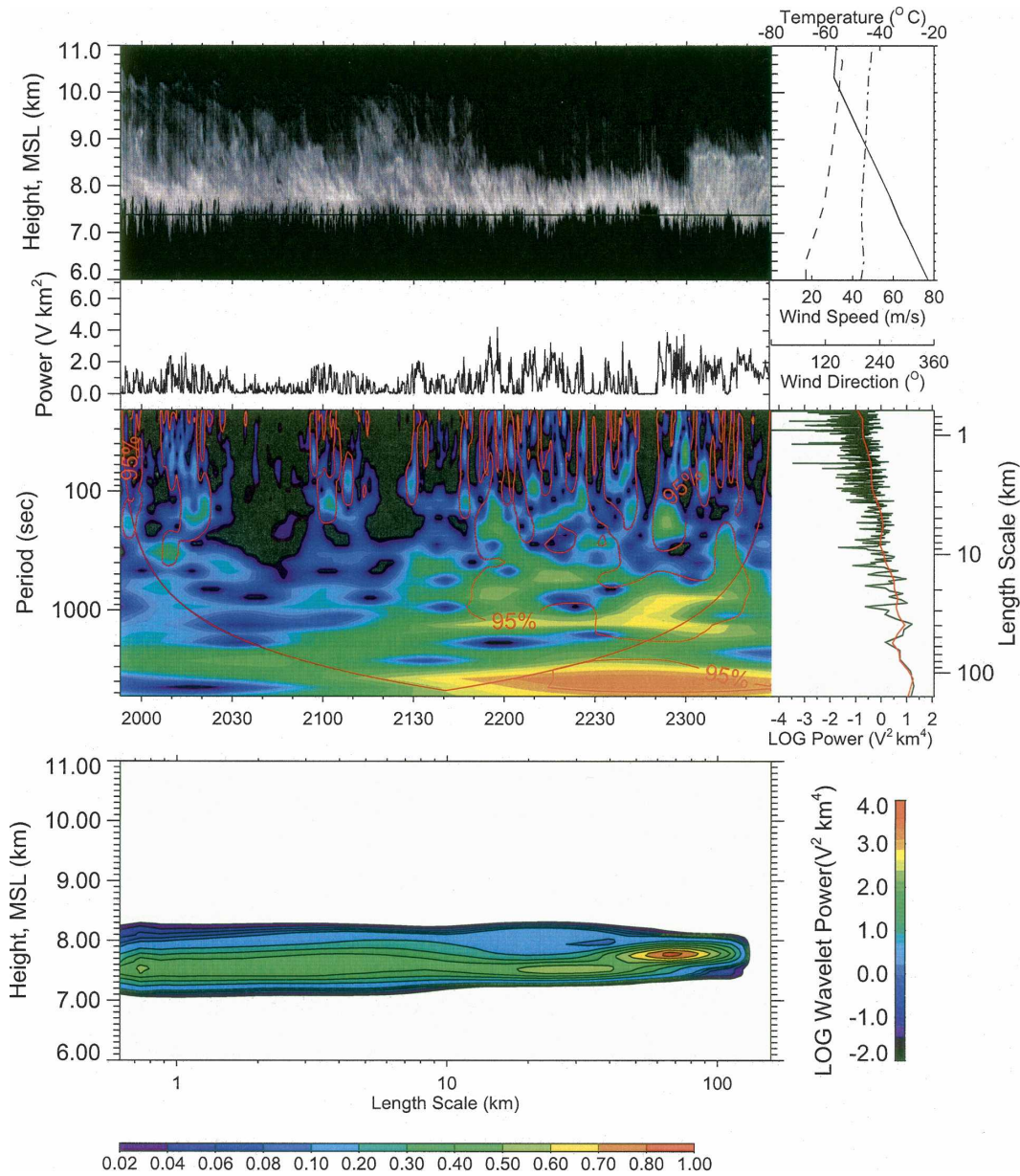


FIG. 6. As in Fig. 4, except that the height of the wavelet analysis is chosen to sample the mammata below the cirrus cloud base, collected on 14 Dec 1993.

shows the result when all the case study findings, regardless of cloud height, are combined.

At the bottom of Fig. 8 is the total number of sample points and those that fall into the 95% and 80% confidence level categories as a function of the length scale calculated from the mean cloud-level wind speed and the length of the observation period. Although the data sample encompasses length scales of from 0.07 to 1000 km, relatively few data points are found in the extremes. Thus, we estimate that the data in the 0.2–200-km length scales bounded by the shaded areas are the

most reliable in our study. The top panel in Fig. 6 shows the total percentage of 95% and 80% confidence level data points relative to the total number of all valid data points given in the bottom graph. This reveals that periodic structures were identified in the cirrus clouds in about 8.4% of the time at the 95% confidence level, or 16.4% at 80%. This value is not strongly dependent on the length scale, although there is a tendency for meso-scale structures to increase with length scales in both cases. The features in the shaded regions are based on relatively small data samples, but may, for example,

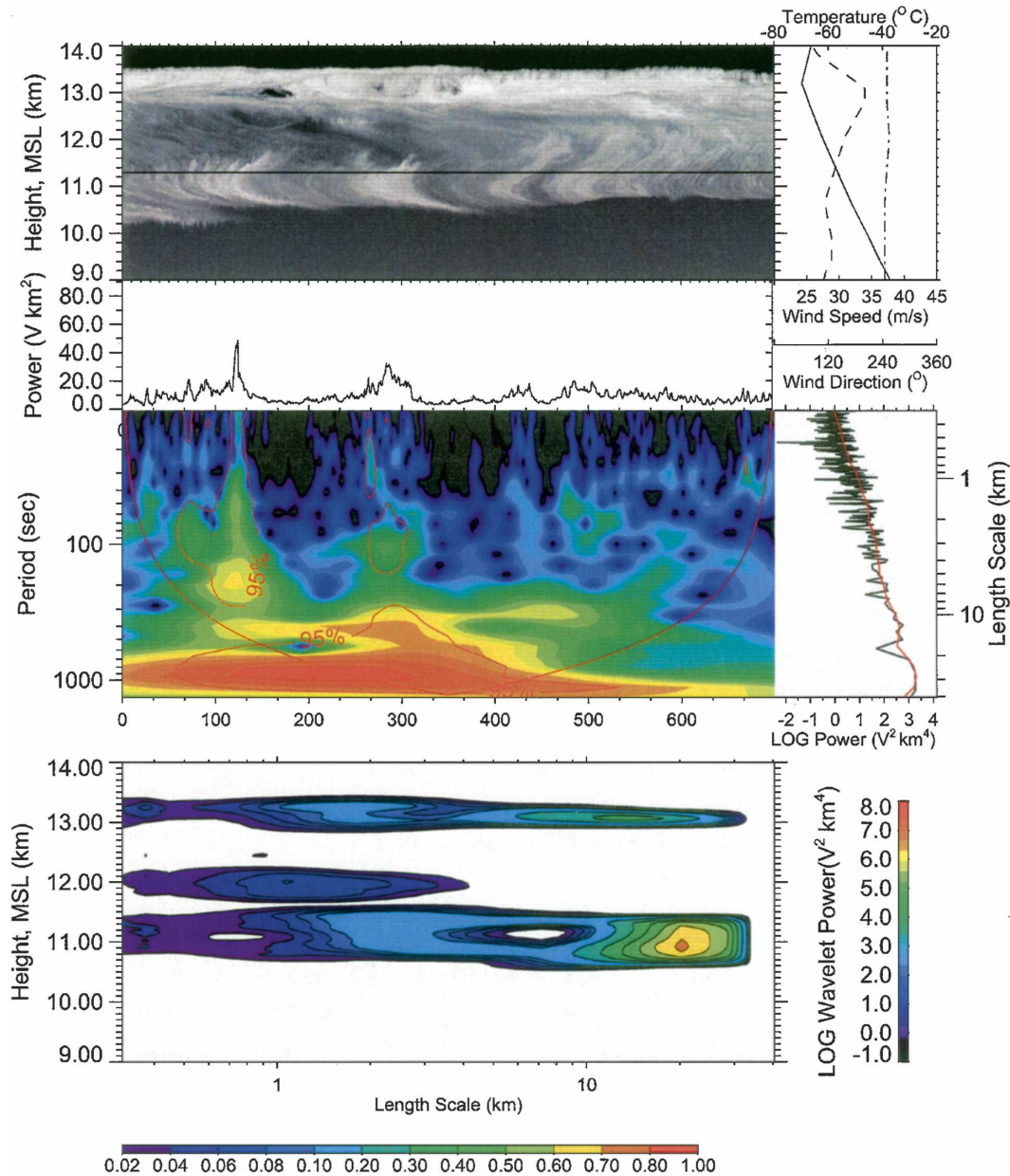


FIG. 7. As in Fig. 4, except that the height of the wavelet analysis is chosen to sample the cirrus uncinus cells and cell complexes, collected on 19 Nov 1999. This analysis is based on higher time (1 s) resolution PDL measurements.

signify the emergence of synoptic-scale cloud structures at right in the longest data records. The results of this analysis for a variety of confidence levels are given in the top row of Table 3.

b. Normalized cloud height results

Numerical model results indicate that cirrus clouds are generally generated near cloud top, where water vapor supersaturations are the greatest in ascending air,

and the ice crystals nucleated there subsequently grow while sedimenting through the still ice-supersaturated air below until encountering subsaturated conditions and gradually evaporating (Khvorostyanov and Sassen 1998). Thus, generating cells and complexes of these units should be found near cloud top (and at other favorable locations), while mammata will emerge at the cloud-base position under the proper conditions. To search for the occurrences of these and other wave pat-

TABLE 2. Mean and observed ranges (in parentheses) of scale lengths and other properties associated with cirrus cloud-scale structures.

Cloud structure	Height (km)	Temperature (°C)	Distance (km)	Depth (km)	Length scale (km)
Uncinus cells	11.5	-60.0	30.0-40.0	—	~2.0 (1.0-4.0)
KH waves	9.8	-45.9	45.2	0.60	4.4 (0.9-11)
Mammata	6.0	-22.1	137.2	0.67	2.9 (0.5-8.0)

terns in cirrus, we also examine our results as a function of relative cloud height (i.e., cloud base = 0 and cloud top = 1.0).

To accomplish this a further subset of lidar backscatter data was created, which excluded those cirrus that displayed irregular or strongly sloping cloud top or base heights over time. This resulted in keeping ~60% of the total dataset, or 309 separate case studies. The relative cloud depth was then divided into four height intervals, which are given in Table 3 below the total results. (This particular division yielded the strongest indications of height dependencies.) These findings also show that the frequency of identified cloud structures increases as the confidence level is lowered, and that

it is the middle-to-lower portions of the cirrus layers that display the highest frequencies of periodic structures.

In Fig. 9 we give examples of the appearance of the height-normalized results plotted against length scale for the 95% and 80% confidence levels. The percentage of data points showing periodic cloud features at these confidence levels relative to the total height-normalized sample is displayed using the inserted grayscale with contours, while average values in each of the four height divisions are given in the panels at right. Clearly, the relaxed confidence level results display increased cloud regions with identified structures, particularly in the 10%-60% portion of the lower cloud (see panels at right).

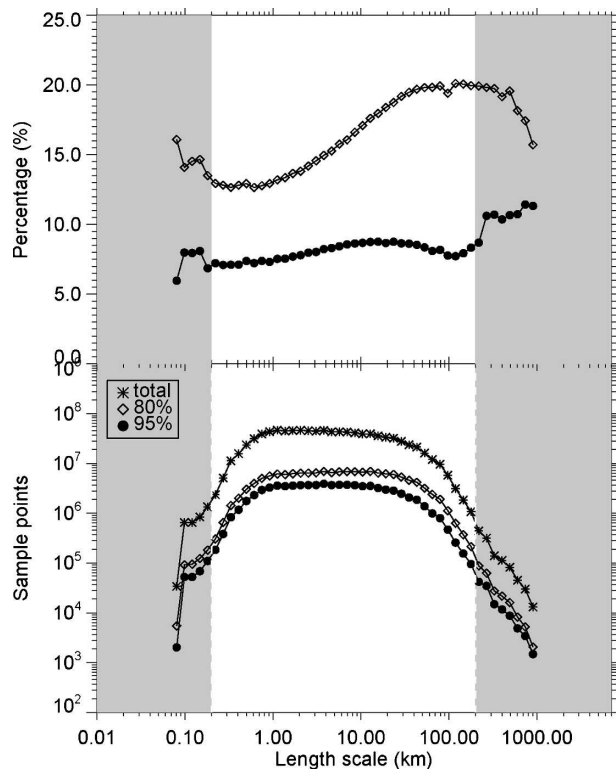


FIG. 8. Total number of (bottom) all data points and possible 95% and 80% confidence level points, compared with (top) the percentage of valid 95% and 80% confidence level points as a function of length scale. A data point here refers to each 37.5-m averaged height lidar signal of each lidar shot.

c. Cirrus cloud optical depth variability results

A direct measure of cirrus cloud optical variability is given in Fig. 10, which shows the term σ/τ plotted against the mean τ derived from the LIRAD approach for each cirrus case. Although significant scatter is apparent in Fig. 10, there is no clear dependence of cirrus optical variability on mean τ . In other words, these cirrus clouds contain inhomogeneities regardless of their overall impact on radiative transfer. Although the dataset is relative small for $\tau > 1.0$, the apparent decreasing trend in this region may represent a saturation effect in radiative transfer, where the impact of cloud structures in physically and optically thicker cirrus are less noticeable. It is important to note that this inherent optical variability is present even if the cirrus structural variations are not periodic.

TABLE 3. Percentage of cirrus cloud data points falling into the indicated wavelet confidence levels (relative to the total valid sample) for the total sample and the height-normalized cirrus layer subset.

Cloud portion	95%	90%	85%	80%	70%	50%
Total	8.4	11.5	14.1	16.5	21.3	30.8
Top 80%-100%	6.6	9.2	11.3	13.5	17.3	23.9
Middle 60%-80%	7.2	10.6	14.1	17.6	24.7	38.3
Middle 10%-60%	13.5	19.5	24.3	28.7	36.6	50.8
Bottom 0%-10%	5.0	9.6	11.3	13.0	15.7	14.9

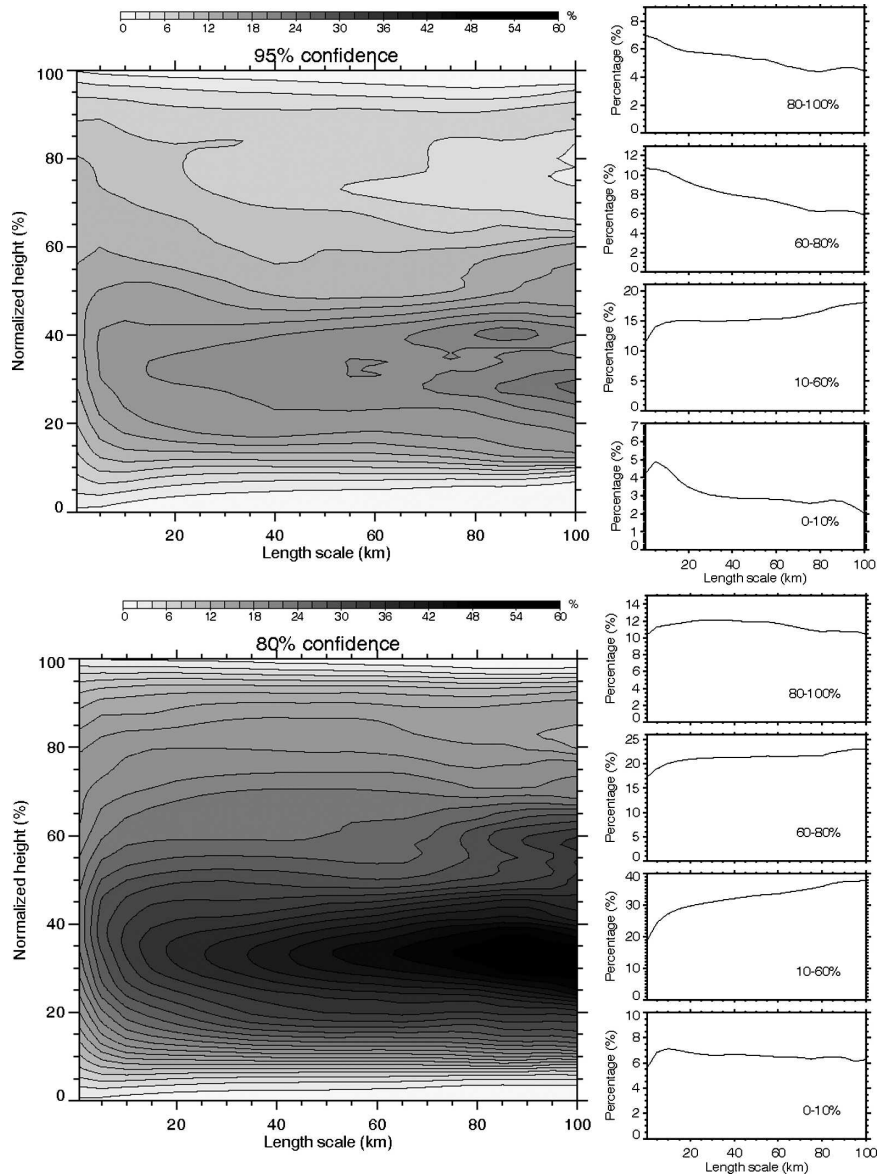


FIG. 9. Cloud height normalized results in terms of the percent of the total sample plotted against length scale for confidence levels of (top) 95% and (bottom) 80%. (right) The average values for the different normalized cloud height regions.

8. Discussion and conclusions

The wavelet analysis presented here indicates that the periodic structures identified through time variations in lidar backscatter profiles are commonly found in cirrus, although various factors may contribute to limiting the effectiveness of this approach when dealing with extended ground-based lidar data time series. This may be particularly true for mesoscale structures because of evolving synoptic cirrus-level wind conditions and feedbacks to cirrus structures induced by dissipative (i.e., turbulence) and radiative effects. It must be

acknowledged that the violation of the Taylor hypothesis, which assumes the mean advection speed is greater than the speed at which cloud structures evolve into different structures, may lead to ambiguous results under conditions involving long data records with changing wind conditions within the cirrus. A nonperiodicity in wave patterns may also result from interference effects from coexisting gravity waves of different wavelengths (Demoz et al. 1998). Nonetheless, at wavelet confidence levels of 95% and 80%, we find that 8.4% and 16.4% of the dataset reveal periodic cloud structural variations.

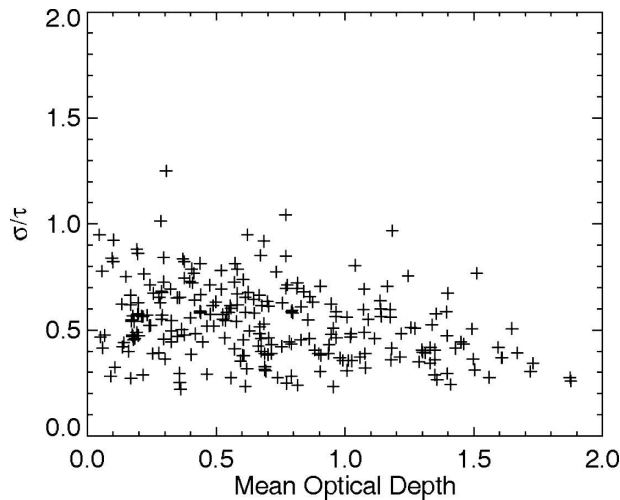


FIG. 10. Shown is the variability in cirrus cloud optical depth τ as expressed by the ratio of the std dev σ to the mean τ for each cirrus cloud case.

Although many cirrus cloud systems do not contain regular cloud organizations, variations in laser (or sunlight) scattering, whether periodic or random, are crucial for understanding the cirrus radiative transfer through appropriate subgrid-scale parameterizations in models. Certainly, visual examination of the entire lidar dataset reveals that few of the cirrus layers studied from FARS can be considered to be optically homogenous over the typical 3-h observation period, suggesting that aperiodic structures (unidentifiable with wavelet analysis) are dominant though locally periodic structures are common in cirrus. This is supported by the results of the LIRAD analysis (Fig. 10) that shows inherent cloud optical variability irrespective of the mean τ .

The locally periodic cloud structures that are evident in the cirrus lidar data are cloud-top cirrus uncinus cells, cloud-base cirrus mammata, and KH waves that tend to be embedded in the cirrus. Table 2 provides the typical vertical depths and length scales for the former cloud-scale structures derived from a large cirrus sample. Despite the different formation mechanisms, all three have similar average length scales, or wavelengths, in the 2.0–4.4-km range. Whereas cirrus mammata tend to occur over large cloud regions, KH waves occur in limited packets with typically only several waves. Importantly, the wavelet analysis has been successful in showing that these distinct cloud-scale phenomena can coexist in a given cirrus cloud.

The wavelet analysis reveals that the normalized percentage of identified periodic structures is relatively insensitive to scale over the 0.2–200-km range of wavelength scales considered valid, although it is indicated that (particularly at more relaxed confidence levels)

mesoscale organizations tend to occur more frequently with increasing length scale. Thus, there do not appear to be any strongly favored length scales for the wave motions responsible for cirrus cloud structures over the 0.2–200-km range: the relative frequency of cloud (~ 1 to 10 km) scale features merges gradually with the gravity wave-driven mesoscale structures at longer length scales.

The analysis of a further subset of relatively uniform cirrus layers, normalized by relative cloud height intervals (Table 3), reveals a tendency for the middle to lower portions of cirrus to contain the greatest amounts of identified cloud structures at all confidence levels. Both visual examination of lidar cloud displays and our statistical analysis indicate that mesoscale cloud organizations tend to be most apparent at middle to low cloud levels. A common cirrus cloud mesoscale structure involves the organization of cloud-top uncinus cells with their series of precipitation fall shafts trailing below. This often produces a serrated tooth-like appearance, with the cloud streaks penetrating to various levels below until complete evaporation occurs. Dynamical processes, such as evaporative cooling, and downdrafts and compensating updrafts, may play a role in organizing the numerous individual fall streaks descending from cloud top into mesoscale cloud features, similar to single cirrus uncinus or mammata formation but on a much larger scale. These frequent mesoscale structures correspond to the mesoscale uncinus complexes first noted in Sassen et al. (1989).

We conclude that the midlatitude cirrus clouds studied at FARS are predominantly optically inhomogeneous clouds. This is basically a result of the cloud formation processes acting in these clouds, so the optical variability in cirrus may vary to some degree with geographic location and the corresponding weather conditions (Sassen and Campbell 2001). It seems, not surprisingly, that the PPH assumption is untenable for cirrus over the ~ 0.2 –200-km cloud length scales considered here because of the inherent variability of cirrus cloud structure and the corresponding optical depth.

Acknowledgments. This work has been supported by the National Science Foundation Grant ATM-0296190 and Department of Energy Grant DE-FG02-03ER63530 from the Atmospheric Radiation Measurement Program. Wavelet software was provided by C. Torrence and G. P. Compo, and is available online at <http://paos.colorado.edu/research/wavelets/>.

APPENDIX

Wavelength Confidence Level Testing

In view of the wavelet analysis uncertainty discussion in section 4d, we present here an analysis of a selected

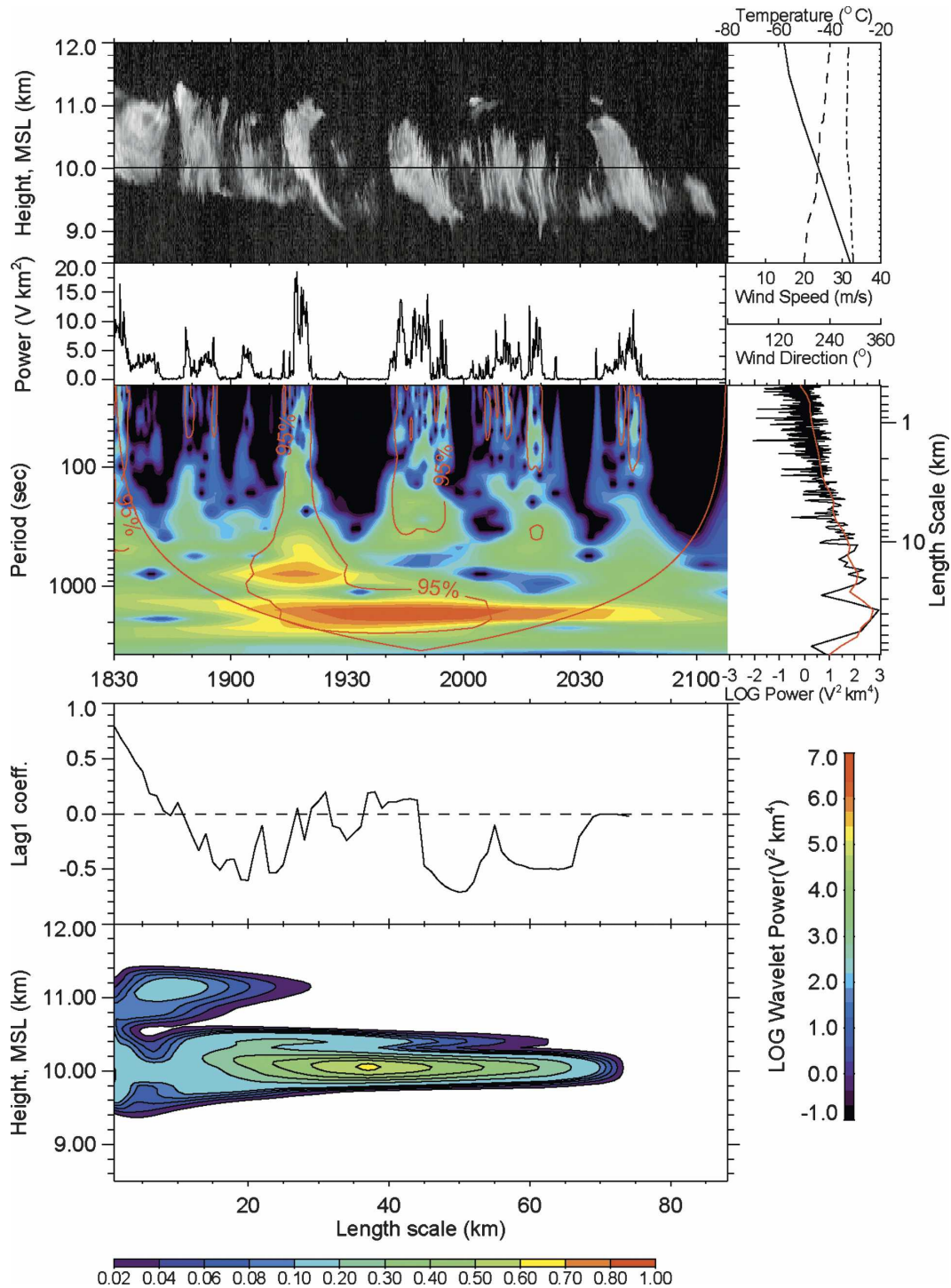


FIG. A1. As in Fig. 4, except that the wavelet analysis is based on (a) 95% and (b) 80% confidence levels, and the results of the corresponding autocorrelation analysis (Lag1 coefficient) of vertically integrated lidar signal are also shown. Cirrus cloud lidar data were collected from FARS on 14 Oct 1997.

case study that provides an opportunity to evaluate the meaningfulness of a wavelet analysis confidence level that is appropriate for identifying valid periodic structures in cirrus clouds. (Also refer to the several case

studies given in Figs. 4–7.) In Figs. A1a,b are shown wavelet analyses of a cirrus layer at confidence levels of 95% and 80%, along with supplementary environmental, and global, Fourier, and autocorrelation informa-

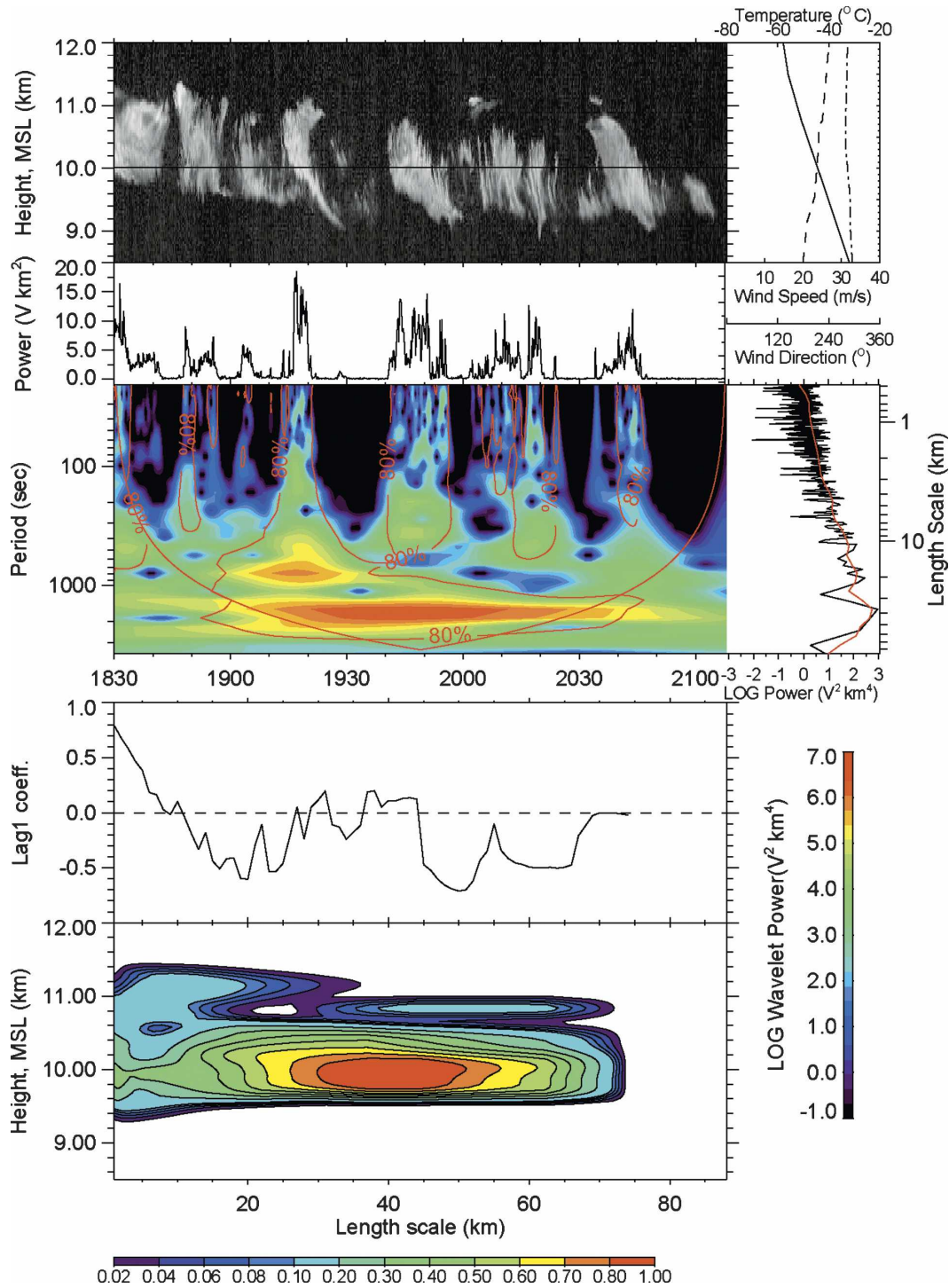


FIG. A1. (Continued)

tion. This cloud was selected because it visually suggests both mesoscale (at ~15 min and/or 30 min) cloud variations and much smaller cloud-scale features due to uncinus structures. Comparing the red-outlined regions at the selected height slice at 95% and 80% confidence

levels shows that the differences are not substantial, and both are in line with the Fourier, global wavelet, and autocorrelation results included in the Lag1 coefficient panel.

Even using visual inspection, however, there is no

strict standard to determine if clouds contain periodic structures or not. Since the ultimate purpose of our wavelet analysis is to quantitatively identify structures in a frequency domain, it is important to develop strategies for deciding whether a particular wavelet is to be omitted on the grounds that noise or random signal variations alone could account for a particular computed value. In other words, creating confidence limits for the wavelet power minimizes errors caused by signal fluctuations that are not related to actual cloud structures. In this analysis we provide results in Fig. A1 after choosing two different confidence levels to explore the uncertainty that some cloud structures could be missed.

The differences between the 95% and 80% confidence level results can be seen to lie mainly in the cloud areas found to contain valid periodic structures (cf. the bottom 2D panels of Figs. A1a,b). Obviously, at the 80% confidence level, cirrus cloud regions showing periodic or near-periodic cloud structures are enhanced, especially those at the mesoscale. In view of the previous discussions of the effects of cirrus cloud evolution during advection over a ground-based lidar, we conclude that a relaxed confidence level is appropriate particularly for structures that require the analysis of long time periods. A 95% confidence level, on the other hand, works well for identifying localized packets of well-defined structures such as Kelvin–Helmholtz waves (see Fig. 5).

REFERENCES

- Auria, R., and B. Campistron, 1987: Origin of precipitation and dynamic organization in wavelike precipitation bands. *J. Atmos. Sci.*, **44**, 3329–3340.
- Barker, H. W., 1996: A parameterization for computing grid-averaged solar fluxes for inhomogeneous marine boundary layer clouds. I: Methodology and homogeneous biases. *J. Atmos. Sci.*, **53**, 2289–2303.
- Cahalan, R. F., W. Ridgway, W. J. Wiscombe, and T. L. Bell, 1994: The albedo of fractal stratocumulus clouds. *J. Atmos. Sci.*, **51**, 2434–2455.
- Carlin, B., Q. Fu, U. Lohmann, G. G. Mace, K. Sassen, and J. M. Comstock, 2002: High-cloud horizontal inhomogeneity and solar albedo bias. *J. Climate*, **15**, 2321–2339.
- Chatfield, C., 1996: *The Analysis of Time Series: An Introduction*. 5th ed. Chapman and Hall, 283 pp.
- Comstock, J. M., and K. Sassen, 2001: Retrieval of cirrus cloud radiative and backscattering properties using combined lidar and infrared radiometer (LIRAD) measurements. *J. Atmos. Oceanic Technol.*, **18**, 1658–1673.
- Demoz, B. B., D. O’C. Starr, K. R. Chan, and S. W. Bowen, 1998: Wavelet analysis of dynamical processes in cirrus clouds. *Geophys. Res. Lett.*, **25**, 1347–1350.
- Dunkerton, T. J., 1997: Shear instability of internal inertia gravity waves. *J. Atmos. Sci.*, **54**, 1628–1641.
- Farge, M., 1992: Wavelet transforms and their applications to turbulence. *Annu. Rev. Fluid Mech.*, **24**, 395–457.
- Fritts, D. C., and M. J. Alexander, 2003: Gravity wave dynamics and effects in the middle atmosphere. *Rev. Geophys.*, **41**, 1003, doi:10.1029/2001RG000106.
- Gilman, D. L., F. J. Fuglister, and J. M. Mitchel Jr., 1963: On the power spectrum of “red noise.” *J. Atmos. Sci.*, **20**, 182–184.
- Grund, C. J., and E. W. Eloranta, 1990: The 27–28 October 1986 FIRE IFO cirrus case study: Cloud optical properties determined by high spectral resolution lidar. *Mon. Wea. Rev.*, **118**, 2344–2355.
- Gultepe, I., and D. O’C. Starr, 1995: Dynamical structure and turbulence in cirrus clouds: Aircraft observations during FIRE. *J. Atmos. Sci.*, **52**, 4159–4182.
- , —, A. J. Heymsfield, T. Uttal, T. P. Ackerman, and D. Westphal, 1995: Dynamical characteristics of cirrus clouds from aircraft and radar observations in micro and mesogamma scales. *J. Atmos. Sci.*, **52**, 4060–4078.
- Harshvardhan, and D. A. Randall, 1985: Comments on “The parameterization of radiation for numerical weather prediction and climate models.” *Mon. Wea. Rev.*, **113**, 1832–1833.
- Heymsfield, A. J., 1975: Cirrus uncinus generating cells and the evolution of cirriform clouds. Part II: The structure and circulations of the cirrus uncinus generating head. *J. Atmos. Sci.*, **32**, 809–819.
- Khvorostyanov, V. I., and K. Sassen, 1998: Cirrus cloud simulation using explicit microphysics and radiation. Part II: Microphysics, vapor and mass budgets, and optical and radiative properties. *J. Atmos. Sci.*, **55**, 1822–1845.
- Lane, T. P., J. D. Dolye, R. Plougonven, M. A. Shapiro, and R. D. Sharman, 2004: Observations and numerical simulations of inertia-gravity waves and shearing instabilities in the vicinity of a jet stream. *J. Atmos. Sci.*, **61**, 2692–2706.
- Liou, K.-N., and N. Rao, 1996: Radiative transfer in cirrus clouds. Part IV: On cloud geometry, inhomogeneity and absorption. *J. Atmos. Sci.*, **53**, 3046–3065.
- Ludlam, F. H., 1948: The forms of ice clouds. *Quart. J. Roy. Meteor. Soc.*, **74**, 39–56.
- , 1956: The forms of ice clouds: II. *Quart. J. Roy. Meteor. Soc.*, **82**, 257–265.
- Nastrom, G. D., and D. C. Fritts, 1992: Sources of mesoscale variability of gravity waves. Part I: Topographic excitation. *J. Atmos. Sci.*, **49**, 101–110.
- Oddie, B. C. V., 1959: Some cirrus observations made by the Westminster Shiant Isles Expedition. *Weather*, **4**, 204–208.
- Percival, D. B., 1995: On estimation of the wavelet variance. *Biometrika*, **82**, 619–631.
- Qiu, L.-J., and M.-H. Er, 1995: Wavelet spectrogram of noisy signals. *Int. J. Electr.*, **79**, 665–677.
- Quante, M., and D. O’C. Starr, 2002: Dynamical process in cirrus clouds: A review of observational results. *Cirrus*, D. K. Lynch et al., Eds., Oxford University Press, 346–374.
- , G. Teschke, M. Zhariy, P. Maaß, and K. Sassen, 2002: Extraction and analysis of structural features in cloud radar and lidar data using wavelet based methods. *Proc. Second European Conf. on Radar Meteorology*, Delft, Netherlands, European Meteorological Society, 95–103.
- Reuss, J. H., 1967: Großräumige Cirrus-Bänder als Merkmale von Luftmassengrenzen der hohen Troposphäre und ihrer Eigenschaften. *Beitr. Phys. Atmos.*, **36**, 7–15.
- Sassen, K., 1995: Lidar cloud research. *Rev. Laser Eng.*, **23**, 148–153.
- , 2002: Cirrus clouds: A modern perspective. *Cirrus*, D. K. Lynch et al., Eds., Oxford University Press, 11–40.
- , and J. R. Campbell, 2001: A midlatitude cirrus cloud clima-

- tology from the Facility for Atmospheric Remote Sensing. Part I: Macrophysical and synoptic properties. *J. Atmos. Sci.*, **58**, 481–496.
- , and S. Benson, 2001: A midlatitude cirrus cloud climatology from the Facility for Atmospheric Remote Sensing. Part II: Microphysical properties derived from lidar depolarization. *J. Atmos. Sci.*, **58**, 2103–2112.
- , and J. M. Comstock, 2001: A midlatitude cirrus cloud climatology from the Facility for Atmospheric Remote Sensing. Part III: Radiative properties. *J. Atmos. Sci.*, **58**, 2113–2127.
- , D. O'C. Starr, and T. Uttal, 1989: Mesoscale and microscale structure of cirrus clouds: Three case studies. *J. Atmos. Sci.*, **46**, 371–396.
- , C. J. Grund, J. D. Spinhirne, M. M. Hardesty, and J. M. Alvarez, 1990: The 27–28 October 1986 FIRE IFO cirrus case study: A five lidar overview of cloud structure and evolution. *Mon. Wea. Rev.*, **118**, 2288–2312.
- , J. M. Comstock, Z. Wang, and G. G. Mace, 2001: Cloud and aerosol research capabilities at FARS: The Facility for Atmospheric Remote Sensing. *Bull. Amer. Meteor. Soc.*, **82**, 1119–1138.
- , W. P. Arnott, D. O'C. Starr, G. G. Mace, Z. Wang, and M. R. Poellot, 2003a: Midlatitude cirrus clouds derived from Hurricane Nora: A case study with implication for ice crystal nucleation and shape. *J. Atmos. Sci.*, **60**, 873–891.
- , J. Zhu, and S. Benson, 2003b: A midlatitude cirrus cloud climatology from the Facility for Atmospheric Remote Sensing. Part IV: Optical displays. *Appl. Opt.*, **42**, 332–341.
- Smith, S. A., and P. R. Jonas, 1997: Wavelet analysis of turbulence in cirrus clouds. *Ann. Geophys.*, **15**, 1447–1456.
- , and A. D. DelGenio, 2001: Analysis of aircraft, radiosonde, and radar observations in cirrus clouds observed during FIRE II: The interaction between environment structure, turbulence, and cloud microphysical properties. *J. Atmos. Sci.*, **58**, 451–461.
- Smith, W. L., Jr., P. F. Hein, and S. K. Cox, 1990: The 27–28 October 1986 FIRE cirrus case study: In situ observation of radiation and dynamic properties of a cirrus cloud layer. *Mon. Wea. Rev.*, **118**, 2389–2401.
- Starr, D. O'C., and D. P. Wylie, 1990: The 27–28 October 1986 FIRE cirrus case study: Meteorology and clouds. *Mon. Wea. Rev.*, **118**, 2259–2287.
- , C. L. Korb, G. K. Schwemmer, and C. Y. Weng, 1992: Observation of height-dependent pressure structure of a strong mesoscale gravity wave. *Mon. Wea. Rev.*, **120**, 2808–2820.
- Stephens, G. L., 1985: Reply. *Mon. Wea. Rev.*, **113**, 1834–1835.
- Torrence, C., and G. P. Compo, 1998: A practical guide to wavelet analysis. *Bull. Amer. Meteor. Soc.*, **79**, 61–78.
- Uccellini, L. W., and S. E. Koch, 1987: The synoptic setting and possible energy sources for mesoscale wave disturbances. *Mon. Wea. Rev.*, **115**, 721–729.
- Várnai, T., and R. Davies, 1999: Effects of cloud heterogeneities on shortwave radiation: Comparison of cloud-top variability and internal heterogeneity. *J. Atmos. Sci.*, **56**, 4206–4224.
- Wang, L., 2004: Midlatitude cirrus cloud structural properties analyzed from the extended Facility for Atmospheric Remote Sensing dataset. Ph.D. dissertation, University of Alaska Fairbanks, 219 pp.
- , and K. Sassen, 2006: Cirrus mammatus properties derived from an extended remote sensing dataset. *J. Atmos. Sci.*, **63**, 712–725.
- Wang, Z., and K. Sassen, 2001: Cloud type and macrophysical property retrieval using multiple remote sensors. *J. Appl. Meteor.*, **40**, 1665–1683.
- Wilks, D. S., 1995: *Statistical Methods in the Atmospheric Sciences: An Introduction*. International Geophysics Series, Vol. 59, Academic Press, 467 pp.
- Yagi, T., 1969: On the relation between the shape of cirrus clouds and the static stability of cloud level—studies of cirrus clouds: Part IV. *J. Meteor. Soc. Japan*, **47**, 59–64.
- , T. Harimaya, and C. Magono, 1968: On the shape and movement of cirrus uncinus clouds by the trigonometric method using stereophotographs—Studies of cirrus clouds: Part II. *J. Meteor. Soc. Japan*, **46**, 266–271.